Sensitivity of acoustic nonlinearity and loss to residual porosity in additively manufactured aluminum*

Ward L. Johnson[a], Jake T. Benzing[a], Orion L. Kafka[a], Newell H. Moser[a], Derek Harris[b], Jeremy J. Iten[b] and Nik W. Hrabe[a]

[a]Applied Chemicals and Materials Division, National Institute of Standards and Technology, 325 Broadway, Boulder CO, 80305, USA
[b]Elementum 3D, 400 Young Court, Erie CO, 80516, USA

ARTICLE INFO

Keywords:
Acoustic nonlinearity
Acoustic loss
Additively manufactured aluminum
Porosity
X-ray computed tomography

ABSTRACT

Acoustic nonlinearity and loss are found to be positively correlated with porosity at industrially relevant levels of less than half a percent in commercially pure aluminum produced by laser powder bed fusion (L-PBF) with several different power levels. The technique employed for acoustic measurements involves nonlinear reverberation spectroscopy (NRS) with noncontacting electromagnetic-acoustic transduction, which offers advantages of adaptability to complex part geometries and short inspection times for industrial qualification of additively manufactured (AM) parts of arbitrary size. Porosity and microstructure are characterized with the Archimedes technique, X-ray computed tomography, and scanning electron microscopy. Fit parameters of nonlinearity and loss *vs.* porosity are found to vary significantly with the height of material in the build, consistent with an hypothesis that the correlations are indirect and involve dislocations as the principal nonlinear/anelastic elements. Nonlinearity and loss decrease with time under acoustic excitation, while being relatively insensitive to pauses in excitation of similar duration, indicating that acoustic excitation at inspection levels induces changes in nonlinear/anelastic defects without predominant involvement of thermal excitation. This remarkable behavior is not seen as a fundamental impediment for the application of the technique to nondestructive AM part qualification because of the brief time required for a measurement.

1. Introduction

Additive manufacturing (AM) of metal parts offers a number of advantages relative to conventional metallurgy and subtractive manufacturing, including near-net-shape fabrication with substantial geometric freedom and flexibility in thermal history at the sub-millimeter scale that enables generation of innovative microstructures. However, commercial manufacturing of AM metal parts with significant mechanical-performance requirements is currently impeded by challenges in part qualification, which partly arise from a lack of well-established nondestructive techniques for quantifying variations in microstructure and defects associated with nonoptimal build parameters [1–3].

An overview of limitations of conventional techniques for nondestructive evaluation (NDE) of AM metals was presented in a NASA Technical Memorandum in 2014 [4], and the general measurement challenges summarized in that report have not been overcome since its publication [3, 5, 6]. These challenges include inapplicability of many inspection techniques to complex AM geometries and/or rough as-built surfaces. In addition, as described in the NASA report, most conventional NDE techniques are designed to detect one or more relatively large "rogue flaws" (*e.g.* cracks) that critically affect mechanical performance, but "finished AM parts typically have greater ranges of porosity and lack of fusion, with defects distributed throughout the part, rendering sizing of relevant flaws or assumption of a single rogue flaw difficult."

One major challenge is evaluation of the volume fraction of heterogeneously distributed pores, which typically have mean dimensions in the low micrometer range. Although X-ray computed microtomography (X-ray CT) can provide three-dimensional representations of pores in AM metals, commercially available lab-based systems cannot provide adequate resolution in parts with geometries that require beam penetration greater than a couple of centimeters. Conventional ultrasonic scattering measurements are relatively insensitive to flaws with dimensions much smaller than the acoustic wavelengths, which are, typically, on the order of half a millimeter at 10 MHz. Acoustic attenuation at higher frequencies, complex AM geometries (including intentional internal air gaps), and rough as-built surfaces also limit the applicability of conventional ultrasonic scattering techniques for characterizing porosity in AM parts [5–7].

Because of the intrinsic challenges of employing ultrasonic scattering to characterize microscale defects in AM materials, current research on acoustic NDE of AM metals includes a focus on linear resonance techniques, which are readily adapted to complex geometries and can detect internal flaws through measurements of shifts in resonant frequency relative to that of an unflawed reference part [8, 9]. A complicating feature of all resonance techniques is that individual modes can be relatively insensitive to flaws that are localized in some regions of a part, as a result of the spatial variation in amplitude of standing waves. Therefore, in cases where flaws are anticipated to be localized in unpredictable regions of AM parts, measurements of multiple resonant modes may be required for reliable detection. This issue has

*This manuscript is a contribution of the National Institute of Standards and Technology and is not subject to copyright in the United States.

wjohnson@boulder.nist.gov (W.L. Johnson)
ORCID(s): 0000-0002-9241-8011 (W.L. Johnson); 0000-0003-2333-8154 (O.L. Kafka)

been explored by McGuigan *et al* [10] and Obaton *et al.* [11] in measurements of Co-Cr-Mo lattice structures with missing struts. Obaton *et al.* [11] successfully applied a machine learning technique to determine acceptance/rejection criteria from measurements of several resonant modes in these structures.

Since resonant frequencies are directly dependent on dimensions and temperature, the precision of linear resonance measurements for flaw detection will be reduced by slight differences in geometry and/or temperature of test and reference parts. With respect to dimensional uncertainty, we note that as-built AM parts generally have less exact tolerances than machined parts.

Uncertainties associated with dimensional variations of AM parts are essentially absent in nonlinear elastic and anelastic (loss) measurements, which are relatively insensitive to small geometry-related shifts in frequency, and resonant implementations of such measurements maintain applicability to complex AM geometries [12]. Elastic nonlinearity and anelasticity have also been found in a number of studies to be more sensitive than linear elasticity to a variety of defects and microstructural features of materials, including cracks, delaminations, dislocations, and precipitates [13–18].

Uncertainties associated with temperature variations are still present with stepped-frequency nonlinear resonance techniques, such as nonlinear resonant ultrasound spectroscopy (NRUS), that measure shifts in resonant frequency *vs.* vibrational amplitude, because these techniques require acquisition of multiple spectra and temperatures can significantly shift between spectra [19, 20]. However, as demonstrated by Johnson [21], uncertainty associated with temperature drift can be much smaller in nonlinear reverberation spectroscopy (NRS), which involves measurements of the amplitude dependence of resonant frequencies over time intervals on the order of the exponential time constant of a single resonant ringdown. The precision of amplitude-dependent frequency shifts measured with NRS was found to exceed NRUS by two orders of magnitude, and this enhancement of precision was attributed primarily to a reduction in uncertainty from temperature drift [21].

In a previous NRS study at NIST, we found positive correlations of resonant acoustic nonlinearity and loss with volume fractions of distributed voids and unmelted powder in 17-4 stainless steel that was additively manufactured in a laser powder-bed fusion (L-PBF) system with a range of intentionally nonoptimal hatch spacings between laser tracks [22]. That study did not identify the physical source of the observed correlation of nonlinearity and loss with porosity and unmelted powder fraction but suggested that the basic nonlinear elements are dislocations.

In this study, we explore correlations of acoustic nonlinearity and loss with distributed residual porosity in an AM alloy with less complex microstructure: single-phase commercially pure aluminum. Parts with nominally identical geometries are manufactured with a range of laser power levels, leading to distributed porosities in an industrially relevant range of 0.08 % to 0.46 % volume fraction. Acoustic nonlinearity is measured with a phase-sensitive NRS technique that employs noncontacting electromagnetic-acoustic transduction [21], acoustic loss is determined from the rate of exponential decay during resonant ringdown, porosity is characterized with Archimedes and X-ray CT techniques, and information on grain structure and pore morphology is obtained from scanning electron microscopy.

2. Specimens

2.1. AM Build

Parts in the form of rectangular blocks were built in an L-PBF system (EOS M290[1]) from commercially pure aluminum powder. The build was performed in an argon atmosphere.

A diagram of the positions of blocks in the AM build is shown in Fig. 1. The area of the build plate is 25 cm × 25 cm. The built parts include two sizes of rectangular blocks with one surface normal parallel to the build direction and cylindrical parts with their cylindrical axes in the build plane (perpendicular to the build direction). The parts included in this study are eight of the larger blocks indicated by numerical labels in Fig. 1. These blocks were removed from the build plate by sawing at the base. The heights of the blocks (parallel to the build direction) were in the range of 30.7 mm to 32.4 mm after removal from the plate. The major lateral dimensions were in the range of 30.1 mm to 30.3 mm, and the minor lateral dimensions were in the range of 25.3 mm to 25.5 mm.

Table 1 lists the power levels J_{L} and laser energy densities employed for each of the additively manufactured blocks shown with labels in the build layout of Fig. 1. Other laser scan parameters are the same for all blocks, including 1270 mm/s velocity v, 0.13 mm hatch spacing H, 0.02 mm overlap, and 7.0 mm stripe width. The thickness h of each powder layer was 30 μm, the plate temperature was 200 °C, and the argon injection pressure was 0.4 mbar. Values of incident laser areal energy density U_{A} and volumetric energy density U_{V} in Table 1 are estimated from the following expressions [23]:

$$U_{\mathrm{A}} = \frac{J_{\mathrm{L}}}{vH} \tag{1}$$

$$U_{\mathrm{V}} = \frac{U_{\mathrm{A}}}{h}\,. \tag{2}$$

2.2. Electrical Discharge Machining

The bottom sawed surface and top as-built surface of each block were removed from each block by cutting off slabs with thicknesses of 1.5 mm to 3.2 mm with electron discharge machining (EDM), leading to a cut height of 26.04 ± 0.01 mm. The two opposite surfaces corresponding to the major lateral dimension were then similarly removed

[1] Identification of commercial products is provided for technical completeness and does not reflect an endorsement by NIST.

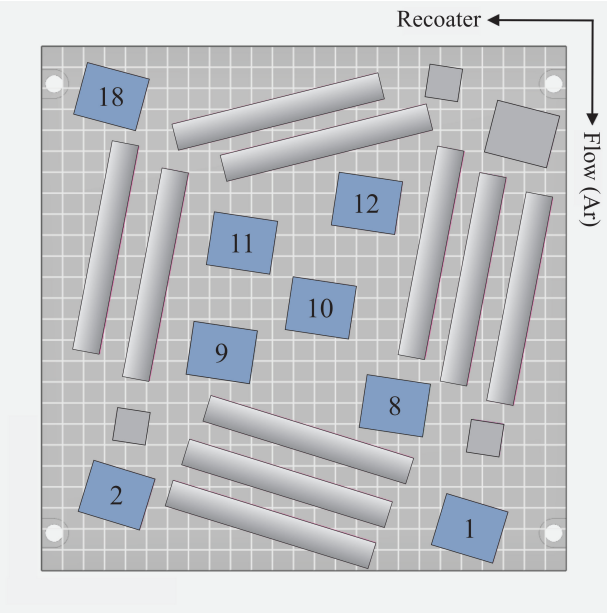

Figure 1: Build layout. Two-dimensional projections of parts are overlaid on a background grid with a spacing of 1 cm. Only the rectangular blocks indicated by numerical labels are included in this study.

Table 1
Laser power J_L, areal energy density U_A, and volume energy density U_V during the additive fabrication of aluminum blocks depicted in the build layout of Fig. 1.

Part #	J_L (W)	U_A (J/mm^2)	U_V (J/mm^3)
1	370	2.24	74.7
2	370	2.24	74.7
8	290	1.76	58.6
9	310	1.88	62.6
10	370	2.24	74.7
11	330	2.00	66.6
12	350	2.12	70.7
18	370	2.24	74.7

by EDM, leading to a lateral dimension of 26.04 ± 0.01 mm. Three cylindrical specimens (for acoustic measurements and X-ray CT) and one rectangular specimen (for scanning electron microscopy) were then cut by EDM from each block with the positions and orientations depicted in Fig. 2. In this figure, the build direction is vertical and the two EDM'd side faces are towards the front and back. Therefore, the lengths of all specimens are 26.04 ± 0.01 mm, and none of the surfaces of the specimens are as-built. The diameters of the cylindrical specimens are 7.995 ± 0.01 mm, except for a narrow axial ridge extending along the entire length on one side (an artifact of EDM cutting) with ∼0.1 mm height and ∼0.2 mm width (comparable to the 0.25 mm EDM wire diameter). On specimens labeled "A" and "B" in Fig. 2, this EDM ridge faces towards the top of the build and, therefore, serves as an indicial feature for determining specimen orientation in X-ray CT.

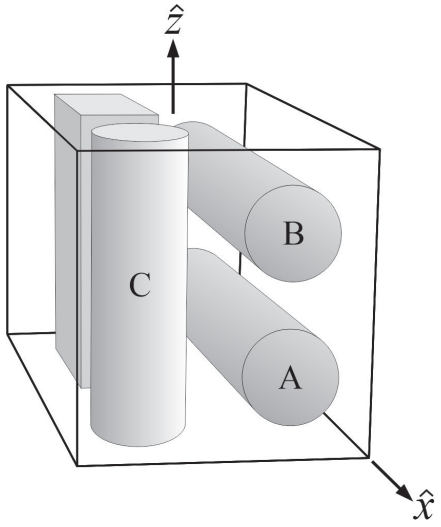

Figure 2: Positions, orientations, and labels of specimens cut by EDM from each of the additively manufactured blocks. The build direction is $\hat{z}$.

2.3. Chemical Composition

The chemical composition of a piece of block 11 that was scrap after EDM cutting of specimens (the slab cut from the side of the block at the front-facing ends of specimens A and B in Fig. 2) was measured with Inductively Coupled Plasma Mass Spectroscopy (ICP-MS, performed by IMR Test Labs). This block was selected for analysis because it was built with a laser power equal to the median of the power levels employed for the specimens (Table 1). Atomic percentages of impurity elements in the aluminum sample were determined to be 0.0005 As, 0.0062 B, 0.0055 Cr, 0.0009 Cu, 0.0876 Fe, 0.0053 Ga, 0.0011 Mn, 0.0011 Mo, 0.0172 Ni, 0.0001 Pb, 0.0436 Si, 0.0001 Sn, 0.0049 Ti, 0.0062 V, 0.0019 Zn, and 0.0004 Zr. Therefore, the total known impurity concentration is 0.337 at.%. Concentrations of Ba, Bi, and W were determined to be below a detection limit of 0.0001 at.%, those of Be, Cd, Co, Ge, Sb, and Sr were below a detection limit of 0.0005 at.%, and that of Li was below a detection limit of 0.002 at.%.

3. Experimental Techniques

3.1. Acoustics

3.1.1. Transduction and Resonant Modes

Resonant vibrational modes of the specimens are excited through noncontacting electromagnetic-acoustic transduction (electromagnetic-acoustic resonance, EMAR). Following the approach described by Johnson [21], a radio-frequency (RF) current through a 153-turn solenoid coil surrounding the specimen is employed to generate near-surface Lorentz forces in the presence of a uniform magnetic field **B** produced by a Halbach magnet (Magnetic Solutions

Ltd., Dublin). The magnitude of this field is 0.540 ± 0.005 T, and its direction is perpendicular to the cylindrical axis of the specimen. The length of the coil is (41.0 ± 0.5) mm, approximately 15 mm greater than the length of each of the specimens.

In this configuration, Lorentz forces are approximately axial and opposite in sign on opposite sides of the specimen. These forces strongly couple to modes with predominantly axial displacements and phase variation of 2π around the circumference, corresponding to "axial-shear" (higher-order flexural) modes near cutoff (*i.e.,* with zero axial wavenumber) in infinite cylinders [24, 25], if the excitation frequency is close to that of a resonant frequency of one of these modes. There are multiple resonant modes with this general symmetry, differing in the number of radial nodes. The focus in this study is the second-lowest-frequency degenerate pair of modes of this type, with two radial nodes, including a node extending approximately along the cylinder axis. The amplitude $|u(r,\theta)|$ of axial vibrational displacements of the corresponding infinite-cylinder modes at cutoff is given by

$$|u(r,\theta)| = u_0 J_1(\eta r/a)\cos(\theta - \theta_0), \tag{3}$$

where $\eta = 5.33144$, r is the radial coordinate, a is the cylinder radius, θ is the azimuthal coordinate, and values of the constant θ_0 differ by $\pi/2$ for the two degenerate modes [25]. A contour plot of axial displacements of one of these degenerate modes is shown in Fig. 3, where $\hat{z}$ is the build direction. Displacement patterns of the corresponding modes in finite cylinders are similar to that shown in this figure but have some dependence on x and deviate from purely axial displacement. Numerical calculations of displacements of modes of the specimens in this study are not pursued here but will be presented in a subsequent report.

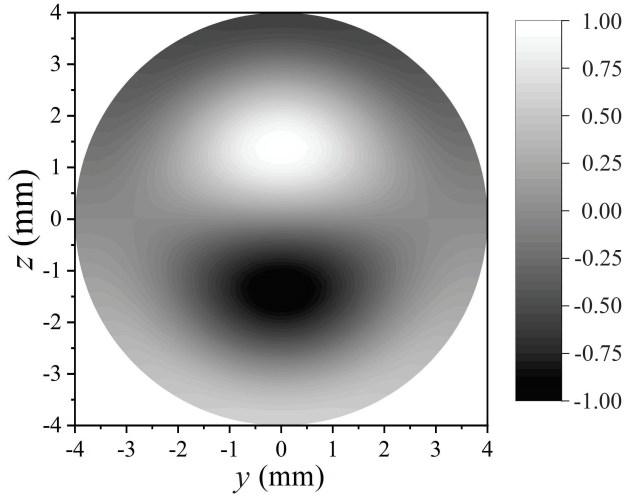

Figure 3: Axial ($\hat{x}$-directed) displacements given by Eq. 3 with $\theta = \arctan(z/y)$ and $\theta_0 = \pi/2$. Values indicated on the color scale are normalized to the maximal displacement.

3.1.2. Electronics

The coil surrounding the specimen is driven by tone bursts with a duration of 2.6 ms and pulse repetition frequency (PRF) of 0.5 Hz that are generated by a gated amplifier (RITEC Inc., Model RAM-5000 SNAP). RF voltages during tone bursts are in the range of ∼210 V to 232 V peak-to-peak with the gated amplifier loaded by the coil with a specimen inserted. Following excitation, the coil is employed to sense resonant vibrations of the specimen through the inverse Lorentz effect. Signals from the coil are passed through BNC cables and a clamped diplexer to an RF receiver in the RITEC system with a bandpass of 0.05 MHz to 20 MHz and, then, to phase detectors that extract the components of the signal that are in phase and out of phase with the reference sine wave that is gated to produce the driving tone burst [21]. These extracted components are passed within the RITEC system through 50 kHz low-pass filters. The total gain from the input of the diplexer (from the coil) to the filtered output of the phase detectors is (20.2 ± 0.2) dB, including negative gain across the diplexer and user-programmed gain of the receiver. The filtered in-phase and out-of-phase outputs from the RITEC system are digitized with a high-speed DAQ device (Measurement Computing USB-1604HS) and passed to a computer for analysis. Additional details of the electronic system are described by Johnson [21]. All setup of programmable parameters of the RITEC system and DAQ acquisition are controlled in real time during measurements with a custom program within the National Instruments LabWindows/CVI ANSI C programming environment.

3.1.3. Initial software processing

After acquiring a series of phase-detector outputs from a specimen and recording associated system parameters, software processing is performed with custom routines in MathCad Prime (PTC). The phase-detector outputs are corrected for previously determined receiver nonlinearity [21], and time-dependent backgrounds acquired with no specimen in the excitation/reception coil are subtracted, leading to in-phase and out-of-phase components $PhDet1(t)$ and $PhDet2(t)$, respectively, where t is time relative to the end of the driving tone burst. For each pair of waveforms, the instantaneous phase $\phi(t)$ of the signal relative to the reference sinusoid and RF amplitude $A_{\mathrm{RF}}(t)$ on the coil during ringdown are calculated from the following relations:

$$\phi(t) = \tan^{-1}(PhDet2(t)/PhDet1(t)), \tag{4}$$

$$A_{\mathrm{RF}}(t) = 10^{-G_{\mathrm{dB}}/20}(PhDet1(t)^2 + PhDet2(t)^2)^{1/2}, \tag{5}$$

where G_{dB} is the total system gain (20.2 dB) from the coil to the input of the DAQ. Values of $\phi(t)$ and $A_{\mathrm{RF}}(t)$ from multiple waveforms are optionally averaged before further analysis [21].

3.1.4. Nonlinear Reverberation Spectroscopy

Subsequent software analysis is performed with custom automated analysis templates in OriginPro (OriginLab). The

instantaneous resonant frequency f during ringdown is calculated from $\phi(t)$ through the following relation [26]:

$$\frac{d\phi(t)}{dt} = 2\pi[f(t) - f_{\mathrm{ref}}]\,, \tag{6}$$

where t is time during ringdown and f_{ref} is the frequency of the driving gated sine wave (tone burst). From this relation, any change in slope of $\phi(t)$ *vs.* t reflects a change in resonant frequency $f(t)$ as the vibrational amplitude decays. This is the principle employed here to characterize specimen nonlinearity.

To enable comparisons of the amplitude dependence of resonant frequencies from multiple waveforms, values of $f(t)$ determined from Eq. 6 are expressed as fractional changes relative to the frequency at a specified value of A_{RF} during ringdown [21].

3.1.5. Acoustic loss

Acoustic loss is quantified as logarithmic decrement δ determined from a linear fit of $\ln(A_{\mathrm{RF}}(t))$ *vs.* t over the time interval starting 1 ms after the end of the tone burst and ending when $A_{\mathrm{RF}}(t)$ drops below 10 mV [21]. The slope of such a fit is δ [27] .

3.1.6. Adjustment of drive frequency

To provide close-to-optimal resonant excitation, drive frequencies are automatically adjusted in real time from one waveform to the next on the basis of real-time waveform analysis employing Eq. 6. For this purpose, a value of average resonant frequency during ringdown is determined under the approximation of negligible amplitude dependence and a corresponding lack of dependence of $d\phi/dt$ and f on t in a given waveform.

3.2. Archimedes density measurements

Density measurements with the Archimedes technique were performed with a fixture on a digital scale with a resolution of 10 μg (Mettler-Toledo AT201). The scale was determined to be accurate at the level of its resolution from measurements of a reference weight (Mettler-Toledo).The Archimedes fixture consists of (1) a platform for dry specimen measurements on an arm supported by the scale above an independently supported beaker containing water purified by reverse osmosis and (2) a platform for immersed measurements suspended by a stainless steel wire with a diameter of 0.073 mm that hangs from the arm. A systematic correction of 2.2 μg to measurements of immersed weights is applied to account for the increase in immersed volume of the suspension wire when a specimen is placed in the water (associated with the rise in water level). Measurements of water temperature are performed with a Type K thermocouple, and the density of air-saturated water is determined from the measured temperature through use of the formulation of Jones and Harris [28].

No corrections for variations in ambient atmospheric pressure were applied to the Archimedes measurements, because such corrections were determined to be insignificant. Considering the reported compressibility of water [28] and typical barometric pressures reported by the National Weather Service for the measurement location (Boulder, CO), the effects of deviations from a standard atmosphere on water density are expected to be on the order of $\pm 5 \times 10^{-7}$ g/cm^3, leading to a contribution to the uncertainty in specimen densities that is approximately two orders of magnitude smaller than other combined uncertainties in the measurements.

Weights of immersed specimens were found to increase slightly with time after initial immersion, (typically by several tenths of a milligram or approximately 0.02 % of the immersed weight). However, weights were found to be stable within the standard deviation of the measurements after a period of approximately ten minutes in which the specimen was removed from and reinserted into the Archimedes beaker several times. The observed behavior of initially increasing weights may arise from dispersal or dissolution of microbubbles on the surfaces of specimens. Motivated by this hypothesis, we tested two techniques on a specimen with relatively high porosity to explore the possibility of actively removing potential microbubbles before Archimedes measurements: 1) sonication in an ultrasonic bath and 2) initial immersion in 80 % ethanol/ 20 % water, which has a lower wetting angle than water. A third test involved 1) placing the specimen on a pedestal above water in a pumpable flask, 2) reducing the pressure in the flask to 9.5 torr with a scroll pump, 3) waiting until bubbling (degassing) of the water ceased, and 4) manually vibrating the flask such that the specimen fell into the water (while still under vacuum). None of these three techniques were found to increase subsequent immersed Archimedes weights (in air-saturated water) beyond that measured after approximately ten minutes of immersion, within the uncertainty of the measurements. Therefore, immersed weights for the results reported here were simply determined from multiple measurements performed after at least an hour of immersion in pure water. Optical microscopy of one of the more porous specimens (8-B) after Archimedes measurements (while still immersed in water) revealed no microbubbles on the surface.

Porosity of the AM specimens is estimated from the measured densities through comparison with a reference density that is partly derived from the measured density of an aluminum specimen with >99.999 % purity. This specimen was manufactured by Materials Research Corporation (MRC) by vacuum melting followed by cold working. Concentrations of impurities in the specimen were determined by the manufacturer from inductively coupled plasma (ICP) and direct current plasma (DCP) spectroscopy to include 1.0 ppm Si, 0.6 ppm Cu, 0.9 ppm Mg, and 0.6 ppm Ca, with other measured elements (Fe, Mn, Cr, Zn, Ti, B, P, Ag, Ga, Ni, Mo, Na, K, and Li) below detection limits that range from 0.1 ppm to 1.0 ppm. From Archimedes measurements, the density of this specimen is determined to be (2.70000 $\pm$ 0.00016) g/cm^3 at (21.4 $\pm$ 0.1) °C, where the indicated uncertainty in density combines standard deviations of multiple measurements of dry and immersed weights and 2.2×10^{-5} g/cm^3 uncertainty in water density

associated with the 0.1 °C uncertainty in water temperature. Compensation for the measured impurities in this specimen, through a procedure similar to that described in the following paragraph for the AM specimens, leads to a density ρ_{pure} of 100 % pure aluminum that is $3{\times}10^{-6}$ g/cm^3 less than the density determined for the MRC specimen, leaving the value of 2.70000 g/cm^3 unchanged to the indicated number of digits. The potential presence of elements in the MRS specimen below the ICP/DCP detection limit also introduces uncertainty. If all of the undetected elements with atomic weights greater than Al in the ICP/DCP measurements were assumed to have concentrations equal to their respective detection limits, this would reduce the impurity-compensated value of ρ_{pure} by 18 μg/cm^3 (an amount one order of magnitude smaller than the uncertainty in the density of the MRC specimen), and the alternate assumption of only the lighter elements being present at their detection limits would have an insignificant effect on ρ_{pure}. Considering such potential contributions, the total uncertainty in ρ_{pure} is estimated to be 0.00018 g/cm^3.

A reference density ρ_{ref} for aluminum with no porosity and the 16 measured impurity concentrations C_i (at.%) of specimen 11-B (Sec. 2.3) is estimated from ρ_{pure} by adjusting this density according to the relative atomic weights A_i of the impurities:

$$\begin{aligned}\rho_{\text{ref}} &= \rho_{\text{pure}}\left[1 + 0.01\sum_{i=1}^{16} C_i\frac{A_i - A_0}{A_0}\right] \\ &= 2.70393\,\text{g/cm}^3, \end{aligned} \tag{7}$$

where A_0 is the atomic mass of Al. Neglecting unknown uncertainty in impurity concentrations, the uncertainty in this value for the reference density of the AM specimens is the same as the uncertainty in ρ_{pure}. If all of the undetected elements with atomic weights greater than Al were to have concentrations equal to their respective ICP-MS detection limits, this would increase the impurity-compensated value of ρ_{ref} by 0.00020 g/cm^3, and the alternate situation of only the lighter elements being present at their detection limits would lead to a negative shift of 0.00005 g/cm^3 in ρ_{ref}. Including such potential systematic error in impurity concentrations, the total uncertainty in ρ_{ref} is estimated to be 0.00038 g/cm^3 (0.014 %). This uncertainty does not consider any dependence of density on microstructure (*e.g.*, grain size), as discussed in Sec. 5.

3.3. X-Ray Computed Microtomography (X-ray CT)

X-ray CT measures 3D structures by reconstructing a series of X-ray projection images: mathematically determining the shapes required to cause the observed projection patterns. Imaging contrast is provided by differences in X-ray attenuation, which is strongly linked to material density. Thus, voids and pores in AM metal are distinguishable, and the volume fraction and morphology of pores can be measured. In this study, three AM cylinders with different porosity were measured for comparison with other measurements. X-ray CT was conducted using a Zeiss Xradia Versa XRM-500 system, and 3201 X-ray projection images were taken over a 360° rotation. The specified accelerating voltage was 80 kV and the tube power was 7 W. An exposure time of 10.5 s was chosen to achieve adequate brilliance at the detector. Reconstructions were conducted using the commercial Zeiss software included with the X-ray CT instrument, Scout-and-Scan Reconstructor (version 14.0.14829).

X-ray CT experiments were conducted with a voxel-edge length of (3.00 ± 0.09) μm, resulting in a reconstructed, cylindrical subvolume of approximately 18.9 mm^3 (edge-length uncertainty is derived from the instrument calibration). Each specimen was mounted such that the cylindrical axis of the reconstructed volume was aligned with the cylindrical axis $\hat{x}$ of the specimen and the y-z planes of reconstructed images are defined to be consistent with those shown in Figs. 2 and 3. The X-ray CT images are reconstructed and exported as grayscale, 16-bit TIFF image stacks. In order to compute porosity, the images are segmented (i.e., converted into black-and-white binary images) using a custom image processing library in Python, based on the SciKit-Image routines [29]. To segment the images, they are converted to 8-bit, and then a nonlocal means denoising filter is applied, followed by the application of a global (Otsu) threshold. One facet of uncertainty in the XCT measurement is the precise choice of threshold value used during segmentation. To ascertain the sensitivity of the measurement to this choice, three segmentations are performed: one with an "optimal" threshold value, one with threshold value 2 gray-levels (in the 8-bit image) above, and another with threshold value 2 gray levels below the "optimal" threshold value. The average of the absolute value of the difference between the "optimal" and perturbed values is deemed the *2-grayvalue sensitivity* due to segmentation and can be thought of as a metric of uncertainty. An example of a reconstructed, grayscale image that has been segmented is shown in the Appendix. Porosity is computed by taking the ratio of black (gas) voxels to the total sum of voxels in the imaged region (*i.e.*, the subvolume of the specimen within the field of view at 3.00 μm voxel-edge length) comprising both black and white (metal) voxels: $porosity = n_{black}/(n_{black} + n_{white})$.

Additional X-ray CT images were collected with a voxel-edge length of (9.25 ± 0.28) μm. At this resolution, the entire diameter of an AM cylinder fits within the field-of-view of the reconstructed X-ray CT images, which corresponds to measuring a region of approximately 470.5 mm^3 of the cylinder. For these lower-magnification measurements, 2401 X-ray projection images were taken over a 360° rotation. The accelerating voltage and tube power were unchanged, but the required exposure time was only 4.5 s. These lower-magnification X-ray CT images were initially used to determine the relative heterogeneity of the pore spatial distribution as well as the upper limits in pore size. Based on these observations, the higher voxel-edge resolution of

3.00 μm was ultimately chosen for primary use in the subsequent analysis in this investigation, since it more accurately captures micro- and meso-scale voids. Further information about the lower-magnification X-ray CT measurements is presented in the Appendix.

3.4. Scanning Electron Microscopy

Samples were prepared for scanning electron microscopy through standard polishing procedures: grinding from 600 grit to 1200 grit using SiC paper, polishing with a 1 μm diamond suspension, and vibratory polishing (24 h) using 50 nm colloidal silica. Backscattered electron (BSE) images were recorded with an annular detector in a field emission scanning electron microscope operated at 20 kV in high current mode with a 60 μm aperture. The lateral dimension of a given grain was measured with standard image processing software. More specifically, after the length-to-pixel ratio was set, a line length tool was used to measure the lateral dimension of each grain across the top row of a given BSE image. The lateral dimension is defined as the length between grain boundaries measured across the horizontal direction of the image. (For AM specimens, this direction is perpendicular to the build direction.) After the entire top row of an image was analyzed, the process was repeated on subsequent rows from top to bottom. Across multiple fields of view, approximately 130 grains were measured for each material condition of interest. An analysis of variance (ANOVA) was completed with commercial software and used to test the null hypothesis that the average grain lateral dimensions were equal across material conditions; significance is defined as $p<0.01$. In addition, secondary electron (SE) images of porosity were recorded with an Everhart-Thornley detector using the same microscope and accelerating voltage as described above.

4. Results

4.1. Archimedes density measurements

Table 2 presents the porosities of the AM specimens based on Archimedes measurements of the densities of these specimens and the reference density ρ_{ref} of nonporous aluminum with the impurity content of block 11 (Secs. 2.3 and 3.2). These porosities are found to be in the range of 0.075 % to 0.456 %. For each orientation, the blocks built with lower laser powers (Table 1) are found to have higher porosity.

In each block, the porosity of specimen B is found to be less than that of specimen A. In other words, porosity is less towards the top of the build (Fig. 2).

4.2. X-ray Computed Microtomography

The X-ray CT measurements of porosity, determined with a voxel-edge length of 3.00 μm, are given in Table 3. The sensitivities of the porosity measurements to a 2-grayvalue difference in segmentation threshold for each specimen are also given in this table. These values indicate that the computed values are relatively insensitive to small changes in the choice of threshold. The values of porosity in Table 3 show the same trend between specimens as the corresponding Archimedes results in Table 2. However, the values in these two tables differ by amounts greater than the combination of the X-ray CT threshold uncertainty and the Archimedes uncertainty ($\pm$ 0.019 %). The magnitude of the differences between the X-ray CT and Archimedes results increases with porosity: 0.034 %, 0.068 %, and 0.145 % volume fraction for 1-B, 11-A, and 8-B, respectively. Potential sources of these discrepancies are discussed in Sec. 5 and Appendix A and include systematic errors in X-ray CT measurements associated with resolution and unrepresentative sampling volumes (both phenomena that have been noted previously [30], although rigorous study of these error sources is a topic of future work).

One benefit of X-ray CT is that the pores that contribute to overall porosity can be easily visualized in detail to provide further context to the measurement. Figure 4 shows examples of images acquired from the low-density specimen 1-B ((a) and (b)) and the higher density specimen 8-B ((c) and (d)). These renderings are effectively a projection of all voids in the scan onto a single plane, and, therefore, may appear to depict far greater porosity than that which is actually present (all of the specimens are $>99.5\%$ dense). The fully closed pores are shown in red for easy identification, and the material is depicted as translucent gray. Although the general morphology of the pores appears to be similar in these two specimens, the difference in total pore volume is visually apparent and quantitatively different.

Table 2
Volume fraction (%) of porosity of specimens determined from Archimedes measurements of the specimens and a reference density ρ_{ref} determined from measurements of cold-worked >99.999 % pure aluminum adjusted for impurities in this material and the AM specimens (Sec. 3.2). Uncertainties are approximately $\pm$ 0.019 % volume fraction for all values.

Block #	Porosity (%)		
	Specimen A	Specimen B	Specimen C
1	0.159	0.114	0.075
2	0.174	0.119	0.133
8	0.456	0.360	0.365
9	0.302	0.229	0.256
10	0.118	0.084	0.163
11	0.244	0.188	0.197
12	0.154	0.140	0.170
18	0.158	0.140	0.136

Table 3
Volume fraction (%) of porosity as measured with X-ray CT using a voxel-edge length of 3.00 μm.

Specimen ID	Porosity (%)	2-grayvalue sensitivity (%)
1-B	0.080	$\pm$0.0027
8-B	0.215	$\pm$0.0070
11-A	0.176	$\pm$0.0050

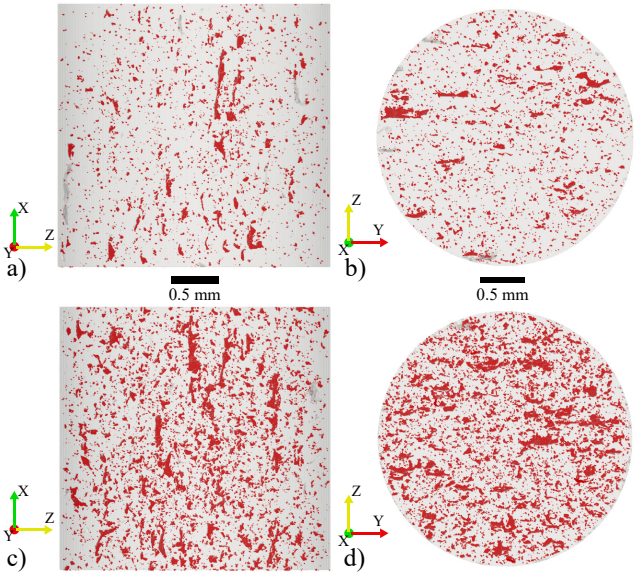

Figure 4: Three-dimensional isometric X-ray CT renderings of regions scanned with a 3.0 μm voxel-edge length, showing two orthogonal views of two different specimens: (a-b) Specimen 1-B with relatively low porosity, and (c-d) Specimen 8-B with relatively high porosity. The metal sample has been made translucent, with fully enclosed pores highlighted in red. In effect, all of the pores in the scanned subvolume are projected onto the orthogonal views. The build direction during the AM process is along the Z-direction (*i.e.*, left to right in (a) and (c), and bottom to top in (b) and (d)).

4.3. Acoustic results

4.3.1. Resonant frequencies

As described in Sec. 3.1.1 the axial-shear modes excited with the selected EMAR configuration would be two-fold degenerate if each specimen had an exactly uniform diameter and transverse elastic isotropy. In the actual specimens described in Sec. 2, a small axial ridge along on one side of each specimen (an EDM artifact) introduces a deviation from cylindrical symmetry. In addition, the microstructures of the specimens with A and B orientations, with cylindrical axes perpendicular to the build direction (Fig. 2), are not isotropic in the cross-sectional planes, as described in Sec. 4.2. As a consequence, the resonant frequencies of the nearly degenerate pair of axial-shear modes in A and B specimens typically differ by approximately 1 %. These frequencies are found to be in the range of 664 kHz to 675 kHz at the beginning of measurements. The excitation of the higher of the two modes in each of these specimens is maximized with the magnetic field approximately parallel to the build direction, and the displacement pattern of this mode has the orientation depicted in Fig. 3.

The axial-shear modes of specimens with the C orientation (Fig. 2) are found to be more close to degenerate, consistent with the cross sections being aligned with the less anisotropic build planes. These specimens have resonant axial-shear frequencies in the range of 675 kHz to 680 kHz.

The results on acoustic nonlinearity and loss presented here are limited to the higher of the two nearly degenerate modes in each specimen.

4.3.2. Acoustic Nonlinearity

Figure 5 shows examples of data on fractional frequency shifts of the higher axial-shear mode of specimen 12-A (673.8 kHz at the beginning of measurements) plotted as a function of A_{RF} during ringdown. These data were acquired during a continuous iterative sequence of tone-burst excitation and waveform acquisition with no change in the position of the specimen in the coil and approximately 10 s between each saved waveform. Between each acquired waveform, the drive frequency was adjusted to approximately match the average resonant frequency during ringdown, as described in Sec. 3.1.6. The three curves in Fig. 5 correspond to waveforms acquired 158 s, 1203 s, and 3200 s after the beginning of repetitive excitation of this resonant mode. The frequency shifts are calculated from Eq. 6 and, for each curve, referenced to the frequency f_{20} at an RF amplitude of 20 mV during ringdown.

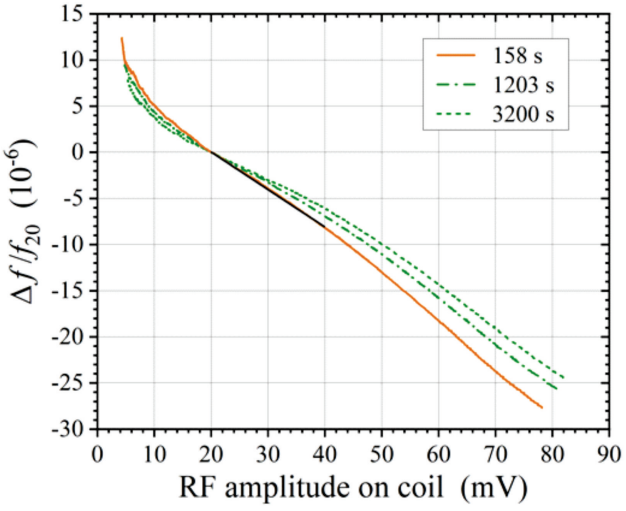

Figure 5: Fractional change in resonant frequency $\Delta f/f_{20}$ of the higher axial-shear mode of specimen 12-A *vs.* RF amplitude A_{RF} on the coil during ringdown, measured 158 s, 1203 s, and 3200 s after the beginning of repetitive excitation of this mode. f_{20} is the frequency determined from the instantaneous time derivative of the phase (Eq. 6) at an RF amplitude of 20 mV during ringdown. Black line: linear least-squares fit of the data acquired at 158 s over the range of RF amplitude from 20 mV to 40 mV.

The data in Fig. 5 show that the resonant frequency is nonconstant as the RF amplitude decays during ringdown, a manifestation of nonlinearity. The slope of each curve in this figure also varies with vibrational amplitude. This amplitude-dependence of the slope is attributed to higher-order terms in the stress/strain relations but not explored in detail here.

Another feature of the data in Fig. 5 is a shifting of the curves with time: the magnitudes of the slopes and

corresponding nonlinearity decrease as the time of waveform acquisition increases from 158 s to 3200 s. Similar time dependence is observed in all of the specimens in this study, and this phenomenon greatly complicates data acquisition and analysis. To enable quantitative analysis of this time dependence and comparisons of nonlinearity of multiple specimens, a least-squares fit is performed of the data from each waveform over the range of A_{RF} from 20 mV to 40 mV, and the slope of this fit is used as a measure of nonlinearity. This relatively narrow range is chosen for the fit because $\Delta f/f_{20}$ is closely approximated as linearly dependent on A_{RF} in this range. An example of such a fit is illustrated in Fig. 5 for the data acquired 158 s after the beginning of excitation of the higher mode. This fit of the amplitude dependence of $\Delta f/f_{20}$ over the selected range is not intended to provide a complete description of the nonlinearity, because it does not consider variations in slope outside this range and the amplitude is expressed as A_{RF}, rather than vibrational strain. We note that other equally appropriate ranges with approximately constant slope in Fig. 5 (*e.g.*, 50 mV to 70 mV) could be selected as a measure of nonlinearity for the purpose of comparing specimens and analyzing the dependence on acquisition time.

In Fig. 6(a), the nonlinearity of the higher axial-shear mode of specimen 12-A is plotted *vs.* waveform acquisition time relative to the time when acoustic excitation was first initiated after manufacture and machining of the specimen. For this specimen, the measurements began approximately one year after manufacture. As described above, the nonlinearity is expressed in terms of the slope of a fit of the instantaneous resonant frequency *vs.* A_{RF} between 20 mV and 40 mV. Before acquiring the data represented in this figure, the azimuthal orientation and frequency were adjusted to briefly excite the higher mode, and, then, excitation of this mode was minimized by adjusting the azimuthal orientation of the coil/sample. The excitation frequency was then switched to the lower axial-shear mode of the nearly degenerate pair (∼ 665.6 kHz), and acoustic measurements of this mode (not shown) were performed over a period of 170 s. After those measurements, excitation of the lower mode was minimized (and, correspondingly, the higher mode near 673.8 kHz was maximized) through azimuthal reorientation of the coil and specimen, and measurements of the higher mode began. The waveform of the higher mode corresponding to the first point plotted in Fig. 6(a) was acquired (681 ± 30) s after the initial turn-on of the gated amplifier with the specimen in the excitation coil.

During the time periods labeled I and II in Fig. 6(a), the excitation of the specimen was, again, switched to the lower mode through minimization of the signal at the higher-mode frequency (by azimuthal reorientation) and locking on to the frequency near 665.6 kHz. Measurements of the lower mode (not shown) were performed during these periods, and, then, excitation was switched back to the higher mode. During the 2501 s period labeled III, the excitation was paused without changing the azimuthal orientation (*i.e.*, the RF excitation from the gated amplifier was turned off). To reduce the

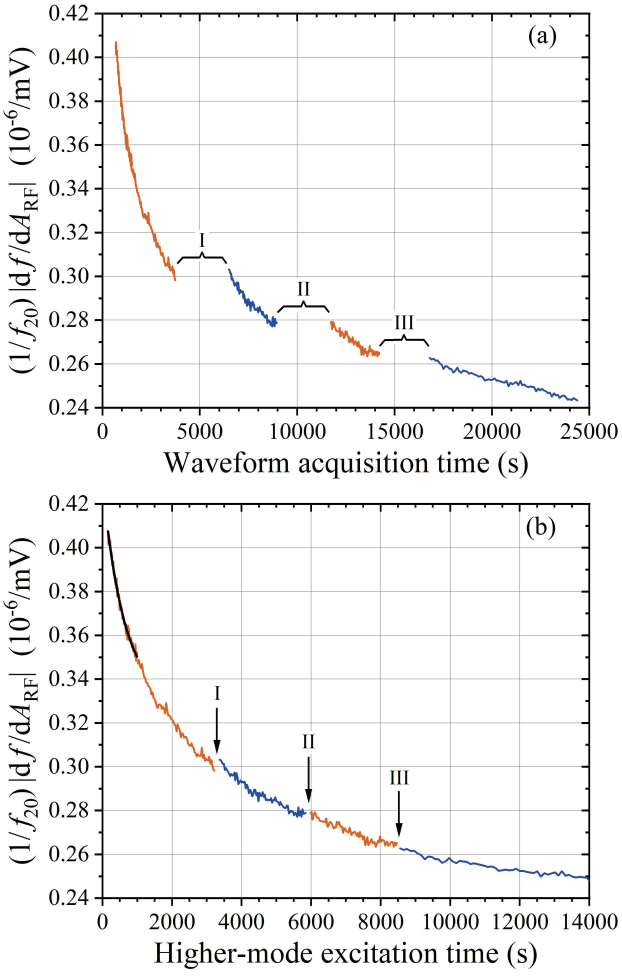

Figure 6: (a) Y-axis: slope of a fit of the fractional shift in resonant frequency f of the higher axial-shear mode (∼ 673.8 kHz) of specimen 12-A *vs.* RF amplitude A_{RF} on the sensing coil, normalized for each waveform to the frequency f_{20} at an RF amplitude of 20 mV. X-axis: time of measurement relative to the time when the driving gated amplifier was turned on. The lower axial-shear mode near 665.6 kHz was excited for (523 ± 30) s before the beginning of the plotted measurements. During periods I and II, the lower axial-shear mode was excited for (2600 ± 20) s and (2629 ± 20) s, respectively. During period III, electromagnetic-acoustic excitation was paused (the gated amplifier was turned off) for (2501 ± 4) s. (b) The same acoustic data plotted *vs.* accumulated time t_{h} of excitation of the higher axial-shear mode. The solid black line is a fit of a decaying exponential function plus a constant to the data over the first 1000 s of higher-mode excitation: $[0.3306 + 0.0996\exp(0.001636\,t_{\mathrm{h}})]\times10^{-6}$/mV.

volume of intermediate data generated during analysis of the waveforms represented in Fig. 6, extracted values of phase *vs.* ringdown time were averaged in sets of 3 waveforms between periods I and III and in sets of 10 waveforms after period III (see Sec. 3.1.3).

The results shown in Fig. 6(a) support the conclusion that excitation of the higher mode affects the nonlinearity

of this mode, while excitation of the lower mode (during periods I and II) or pausing of excitation of the higher mode (during period III) have relatively little effect on the nonlinearity of the higher mode. Fig. 6(b) shows the same acoustic data plotted as a function of total accumulated time t_h of excitation of the higher mode. The approximate continuity of the data in this graph across periods I, II, and III further supports the conclusion that changes in nonlinearity of the measured higher axial-shear mode of this specimen are predominantly dependent on the duration of excitation of this mode.

Instrumental drift should also be considered as a possible source of systematic error contributing to the time dependence of measured nonlinearity shown in Fig. 6. Time-dependent shifts in the curves of resonant frequency *vs.* RF amplitude, as illustrated in Fig. 5, would occur if systematic errors in the phase extracted by the phase detectors vary during ringdown and the magnitude of such errors is dependent on acquisition time. Drifting of receiver gain would also contribute to shifting of the curves through errors in the conversion of the measured phase-detector voltages to RF amplitude on the coil. We consider such electronic effects to be unlikely sources of significant error in measurements of the time dependence of the nonlinearity in Fig. 6, because the low-voltage components of the RITEC system (including phase detectors and receiver) were turned on and thermally equilibrated over a period of approximately 4.5 h before the beginning of acquisition of the data in this figure.

Measurements of the nonlinearity of other specimens also found little effect of pausing excitation of the higher mode or switching to the lower mode for periods of similar duration, with one exception: a shift in nonlinearity was observed in specimen 9-C after a 2500 s pause in excitation, as shown in Fig. 7. These data for 9-C show a transient upward shift after a suspension in excitation near t_h = 2700 s, followed by a return to the approximate trend of the curve before the pause. Similar transient positive shifts in nonlinearity were observed in two other specimens following much longer periods without excitation: specimen 1-A after a pause of 21 days and specimen 2-C after a pause of 39 days.

The solid black line in Fig. 6(b) (for specimen 12-A) is an exponential (plus constant) fit of the acoustic nonlinearity *vs.* higher-mode excitation time t_h before 1000 s. The *y*-intercept of this fit, 0.4302×10^{-6}/mV, is employed to compare the nonlinearity of this specimen with that of other specimens for which the same type of data analysis is performed. In other words, the fit value of $(1/f_{20})\mathrm{d}f/\mathrm{d}A_{\mathrm{RF}}$ at the initiation of higher-mode excitation of each specimen ($t_h = 0$) is used in the following analysis to compare the nonlinearity of specimens and explore correlations of nonlinearity with porosity.

Figure 8 shows fit values of initial $(1/f_{20})\mathrm{d}f/\mathrm{d}A_{\mathrm{RF}}$ (at $t_h = 0$) *vs.* the values of specimen porosity given in Table 2 (Archimedes measurements). The corresponding specimen label for each plotted value (see Figs. 1 and 2) is indicated in this figure, and the three positions/orientations of the specimens within the blocks (labeled A, B, and C in Fig. 2) are plotted with different symbols. Measurements of specimens not represented in this figure either contained insufficient information on higher-mode excitation time before the beginning of measurements (specimens 8-A, 8-C, 9-A, 9-B, 18-A, 18-B, and 18-C) or had substantial interference from nearby resonant modes that made signal analysis unreliable (12-C).

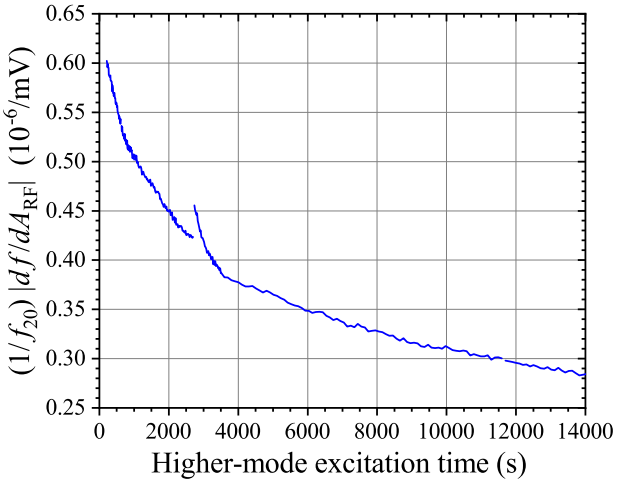

Figure 7: Y-axis: Magnitude of the slope of a fit of the fractional shift in resonant frequency f of the higher axial-shear mode of specimen 9-C *vs.* RF amplitude A_{RF} on the sensing coil, normalized for each waveform to the frequency f_{20} at an RF amplitude of 20 mV. X-axis: Accumulated time t_h of excitation. The discontinuity in the data near 2700 s corresponds to a 2500 s pause in acoustic excitation.

The data in Fig. 8 show positive correlations of initial $|(1/f_{20})\mathrm{d}f/\mathrm{d}A_{RF}|$ with porosity. Results of separate linear regressions of $|(1/f_{20})\mathrm{d}f/\mathrm{d}A_{RF}|$ *vs.* porosity for specimens with each the three orientations are plotted in Fig. 8, and the parameters of these fits are given in Table 4. This table also lists corresponding Anova *p*-values for the null hypothesis that there is no dependence on porosity. From these *p*-values, the correlation of nonlinearity with porosity is found to be significant for the A orientation, very strong for the B orientation, and weaker for the C orientation. The much lower *p*-value for the B orientation is attributed partly to the fact that the data for this orientation includes a specimen with substantially greater porosity (8-B) than that represented in the data for the other two orientations. However, with this data point removed, a *p*-value of 0.007 is obtained for the B orientation, which is still substantially lower than that for the A and C orientations, despite having a smaller range of porosity than those orientations.

The results of the linear regressions in Table 4 also provide evidence for a significant difference in the dependence of nonlinearity on porosity in the A and B specimens: the slopes for these two orientations differ by approximately two

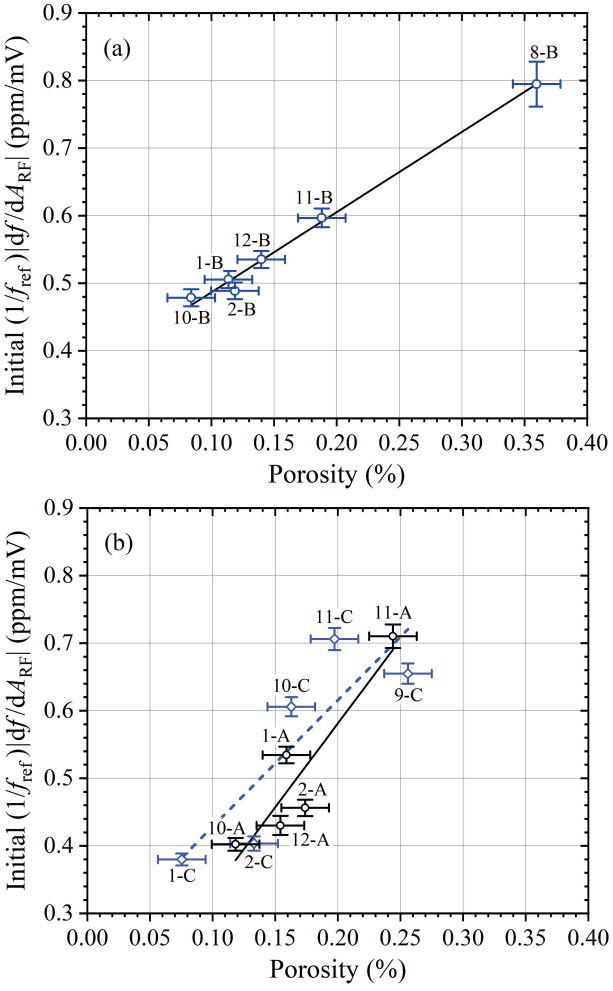

Figure 8: Initial amplitude dependence of resonant frequency ($(1/f_{20})|df/dA_{RF}|$ at $t_h = 0$) *vs.* specimen porosity for (a) B specimens and (b) A and C specimens. Solid and dashed lines are linear regressions of the separate data from the A, B, and C specimens. Uncertainties in porosity are a combination of uncertainties in ρ_{ref} and Archimedes measurements of the AM specimens.

times the combined standard error, and the *y*-intercepts differ by almost three times the combined standard errors. The differences in the fit slopes and intercepts of the B and C data are approximately equal to the combined standard errors, and the fit parameters for the A and C data are not significantly different. Therefore, these data show that the dependence on porosity is different for specimens that only include material from the upper half of the AM build.

4.3.3. Acoustic Loss

The acoustic loss is also found to decrease with excitation time t_h, as illustrated by the data from the higher mode of specimen 12-A plotted in Fig. 9. As with the nonlinearity, periods of excitation of the lower mode (labeled I and II in this figure) and paused excitation (III) had little apparent effect on the loss of this specimen, relative to the effect of higher-mode excitation time. However, measurements of the loss of specimen 9-C revealed a transient increase similar

Table 4
Results of linear regressions of $(1/f_{20})df/dA_{RF}$ *vs.* porosity for each specimen orientation (data plotted in Fig.8). Uncertainites in fit parameters are standard errors.

Specimen orientation	*y*-intercept (10^{-6}/mV)	Slope (10^{-6}/mV/percent)	*p*-value
A	0.09 ± 0.10	2.48 ± 0.59	0.025
B	0.37 ± 0.01	1.19 ± 0.05	2×10^{-5}
C	0.24 ± 0.12	1.87 ± 0.67	0.067

to the pattern of nonlinearity shown in Fig. 7 following the 2500 s pause in excitation. The higher-mode loss of 10-B showed similar transient increases following a one hour pause in excitation and following 690 s of excitation of the lower mode. Longer pauses in excitation of other specimens induced similar patterns in the loss: 1-A (21 days), 2-C (39 days), and 11-A (14 hr).

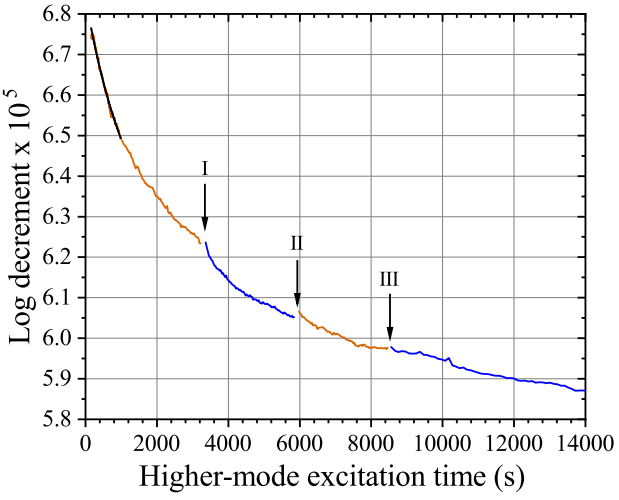

Figure 9: Log decrement of the higher axial-shear mode (~ 673.7 kHz) of specimen 12-A *vs.* accumulated time t_h of excitation of this mode. Periods of lower-mode excitation were introduced at the times indicated by labels I and II, and excitation was paused at the time indicted by label III, as described in the caption to Fig. 6. The solid black line is a fit of a decaying exponential function plus a constant to the data over the first 1000 s of higher-mode excitation.

Following the approach employed in the analysis of nonlinearity (Sec. 4.3.2), the data in Fig. 9 in the range of t_h from 0 s to 1000 s are fit with an exponential plus constant (solid black line) to estimate the log decrement at the beginning of higher-mode excitation. Values determined in this way for all specimens are plotted in Fig. 10 *vs.* porosity determined by the Archimedes method (Sec. 4.1). Linear regressions of these results for each of the three specimen orientations are also shown in this figure, and fit parameters and corresponding Anova *p*-values are presented in Table 5.

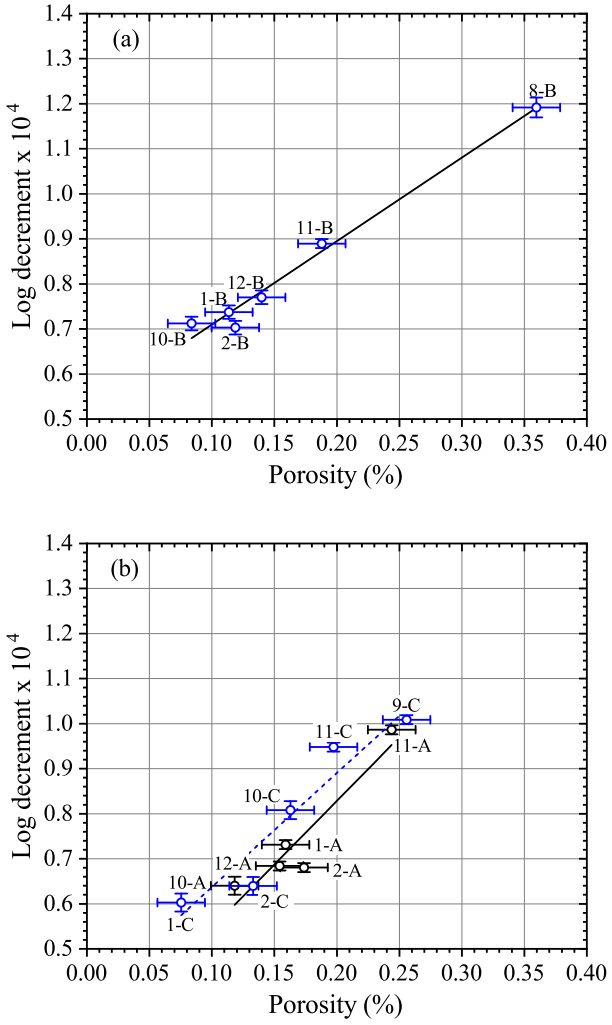

Figure 10: Initial log decrement (at $t_h = 0$) *vs.* specimen porosity for (a) B specimens and (b) A and C specimens. Solid and dashed lines are linear regressions of the separate data from the A, B, and C specimens. Uncertainties in porosity are a combination of uncertainties in ρ_{ref} and Archimedes measurements of the AM specimens

The results for the loss shown in Fig. 10 and Table 5 are similar to those obtained for the nonlinearity (Fig. 8 and Table 4). The slope of the fit for the B orientation differs from that of the A and C orientations by 1.5 and 1.4 times the combined standard errors, respectively, and the slopes determined for the A and C orientations are not significantly different. The *y*-intercept for the B orientation differs from that for the A and C orientations by 2.3 and 1.7 times the combined standard errors, respectively, and the intercepts for the A and C orientations are not significantly different. The correlation determined for the C orientation, with a *p*-value of 0.013, is stronger than that determined for the nonlinearity of specimens with this orientation (*p*-value 0.067, Table 4).

Table 5
Results of linear regressions of log decrement *vs.* porosity for each specimen orientation (data plotted in Fig.10). Uncertainites in fit parameters are standard errors.

Specimen orientation	*y*-intercept	Slope (1/percent)	*p*-value
A	0.26 ± 0.11	2.83 ± 0.63	0.021
B	0.52 ± 0.02	1.85 ± 0.13	1×10^{-4}
C	0.38 ± 0.08	2.53 ± 0.47	0.013

4.4. Scanning electron microscopy

Characteristic BSE images are provided in Fig. 11 to enable a comparison of grain dimensions in the conventionally manufactured pure Al specimen, AM specimen with low porosity (rectangular bar from block 18, Fig. 2), and AM specimen with high porosity (rectangular bar from block 8). The pure Al specimen has a small equiaxed grain structure, whereas the AM specimens have grains that are elongated along the build direction ($\hat{z}$). For each of these specimens, mean lateral dimensions of the grains are determined by measuring the spacings of grain boundaries along multiple lines perpendicular to the build direction in several BSE images, as described in Sec. 3.4. The mean lateral dimensions are determined to be (0.88 ± 0.49) μm for the pure Al specimen, (3.52 ± 1.82) μm for the specimen from block 8, and (3.36 ± 1.70) μm for the specimen from block 18. The difference between the mean lateral dimensions of the pure Al specimen and each AM specimen is significant, but there is no significant difference between the two AM specimens. In addition, characteristic SE images are provided in Fig. 12 to give a 2D qualitative comparison to 3D renderings of porosity as measured by X-Ray CT. These SE images were recorded on samples extracted from rectangular blocks excised from the same parts shown in Fig. 11 (b) and Fig. 11 (c), but the images were acquired on perpendicular planes (the XY plane *vs.* the XZ plane), with respect to the build direction ($\hat{z}$). When comparing similar fields of view, block 8 (Fig. 12 (a)) contains more porosity and larger pores than block 18 (Fig. 12 (b)). The morphology of the pores in these images varies from nearly spherical to more irregular, while showing little or no evidence for levels of complexity that include contacting internal surfaces. Among the pores observed, there is no evidence of entrapment of powder.

5. Discussion

5.1. Porosity

Values of porosity for specimens 1-B, 8-B, and 11-A determined with the Archimedes and X-ray CT techniques (Tables 2 and 3) show the same trends and have similar magnitudes in a range less than 0.5 %. However, the X-ray CT values are all lower than the Archimedes values by amounts greater than the estimated Archimedes uncertainty, and the differences increase with the level of porosity. These

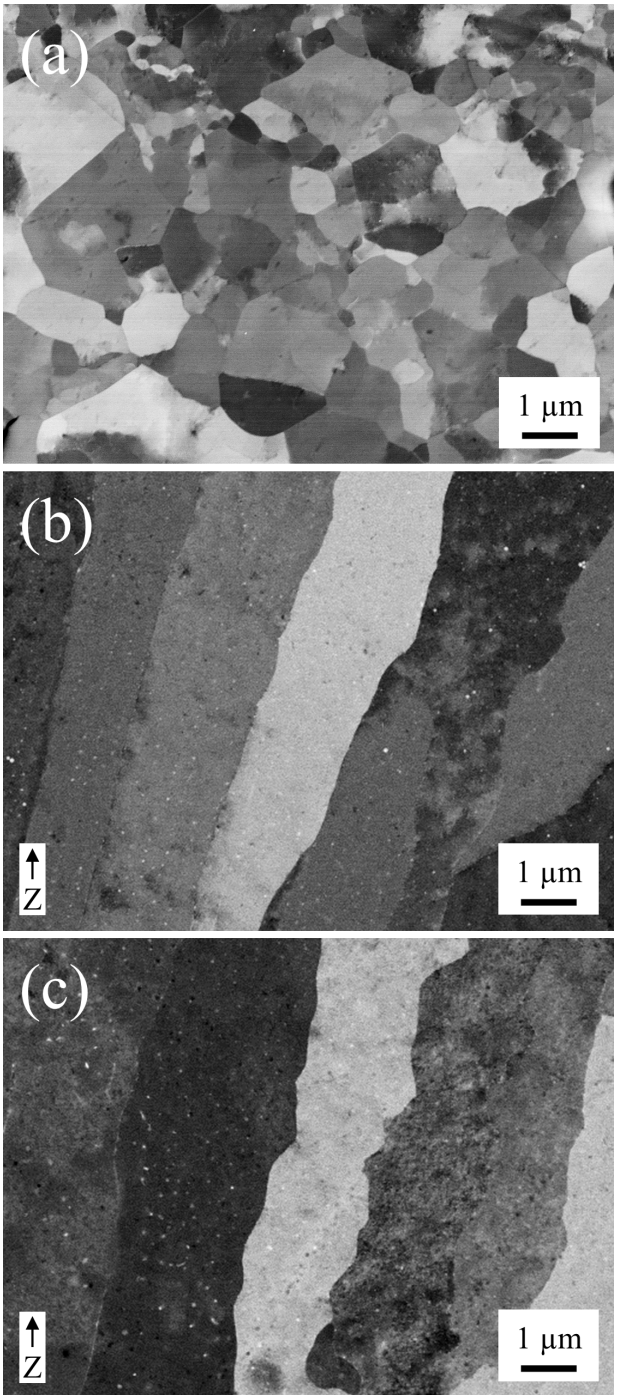

Figure 11: Characteristic BSE images of (a) high purity Al, (b) the rectangular bar from block 8, and (c) the rectangular bar from block 18.

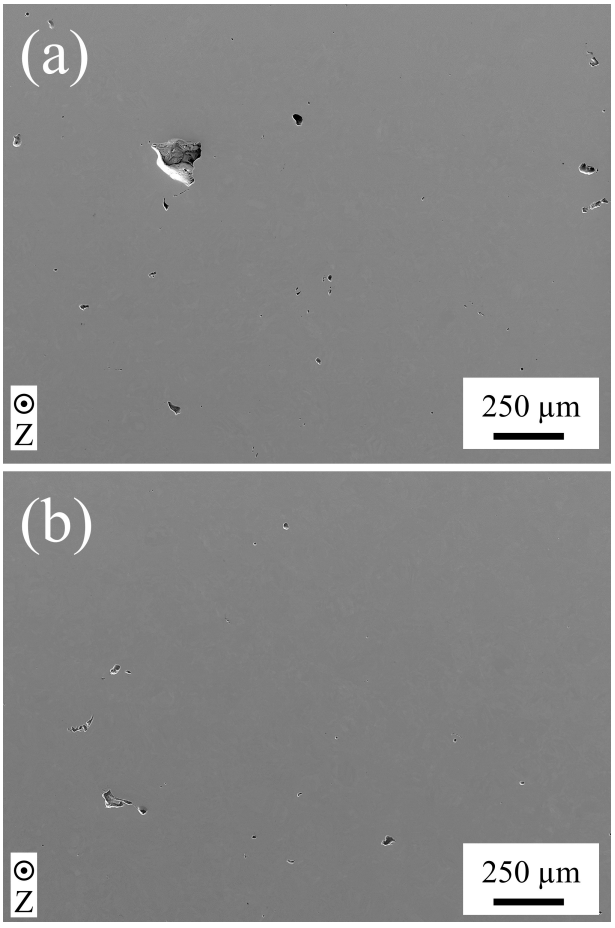

Figure 12: Characteristic secondary electron images: (a) the rectangular bar from block 8, and (b) the rectangular bar from block 18.

discrepancies between the two techniques illustrate the challenges of accurately determining porosity in AM metals at industrially relevant levels of a few tenths of a percent. With respect to X-ray CT measurements, the challenges are associated with finite scan resolution and sampling volume. With respect to Archimedes measurements, the principal challenge is determining a reference density in the absence of porosity. The approach pursued here for the reference of the Archimedes measurements is indirect, involving density measurements of conventional nonporous nearly pure aluminum and calculation of adjustments to this density based on measured trace impurity levels in this material and measured impurity levels in a section of one of the AM blocks with intermediate build parameters. A more direct approach would, perhaps, be measuring the density of a hot isostatically pressed (HIPed) specimen from the same AM build, but we do not know whether this approach would provide greater accuracy of the reference (*e.g.*, whether porosity at the level of hundredths of a percent would remain after HIPing).

The Archimedes and X-ray CT values of porosity for specimen 1-B (0.114 % and 0.080 % volume fraction, Tables 4.1 and 3, respectively) are most close to agreement among the values for the three specimens measured with both techniques. These values would be brought into agreement if ρ_{ref} in the Archimedes calculation were decreased by ~ 0.0009 g/cm^3. This shift is 2.4 times greater than the estimated uncertainty in ρ_{ref}, which is based partly on one standard deviation of the Archimedes weight measurements of the pure aluminum specimen (Sec. 3.2). Systematic error

in ρ_{ref} could arise from a dependence of density on microstructure. One such effect is a dependence on grain size and associated fraction of atoms localized at grain boundaries [31]. As described above (Sec. 4.4), the characteristic lateral dimensions of grains in the AM specimens are found to be approximately 4 times greater than the dimensions of the grains in the pure Al specimen, and the dimensions of the grains in the build direction of the AM specimens are greater. The smaller grains in the pure Al specimen are expected to lead to a downward shift in density [31]. Therefore, the value of ρ_{ref} derived in Sec. 3.2 is expected to be smaller than it should be for aluminum with grain dimensions similar to the AM specimens, and this will lead to calculated values of specimen densities being too high (which is the direction of the discrepancies in the Archimedes and X-ray CT densities). Although such dependence on grain size is normally considered to be negligible for grain sizes above a few tens of nanometers [31], it cannot be ruled out as a significant contribution at the level of the discrepancy of 0.034 % volume fraction between the Archimedes and X-ray CT density measurements for specimen 1-B. Xu *et al.* [31] found, from molecular dynamics calculations, downward shifts in density relative to that of Al single crystal to increase in magnitude with decreasing grain size, following a curve similar to exponential decay of the shift *vs.* mean grain size in a range below 30 nm. Considering the general form of this calculated dependence and an estimate of a 0.4 % shift at 20 nm mean grain size in that study, it would not be surprising if calculations were to find shifts (relative to single crystals) on the order of 0.01 % for Al with grain sizes 40 times greater (on the order of grain sizes measured here in the pure Al specimen (Sec. 4.4)).

Apart from the question of whether grain-size dependence contributes to the discrepancy in Archimedes and X-ray CT densities for specimen 1-B, note that the discrepancies for all three specimens cannot be simultaneously explained by any systematic error in ρ_{ref}, because such an error would lead to an approximately constant shift in porosity determined from the Archimedes measurements. If, for example, ρ_{ref} were shifted downwards to bring the Archimedes and X-ray CT porosities into agreement for specimen 8-B, this would lead to a negative (unphysical) Archimedes value for the porosity of specimen 1-B. On the other hand, if the discrepancies for all three specimens were to be attributed to greater random error in the Archimedes results, the random uncertainty would need to be increased by almost an order of magnitude, and we consider this to be unrealistic. The fact that the discrepancies increase with increasing porosity points to a systematic error. Considering these factors, we conclude that discrepancies between the porosities of 8-B and 11-A determined by the two techniques are primarily associated with systematic error in the X-ray CT measurements.

Potential systematic errors in the X-ray CT measurements of porosity include 1) sampling error, where the subvolume selected for measurements is not sufficiently representative of the entire specimen and 2) resolution error, where either the material/air boundary is inaccurately captured for larger pores or pores with dimensions less than the detection threshold at a given resolution go uncounted. Note that resolution refers to minimally identifiable feature size, which is related to, but not the same as, the voxel-edge length of a scan. These types of systematic error can result in differences in porosities determined with Archimedes and X-ray CT techniques, as well as relative shifts in values determined by X-ray CT for specimens with different levels of porosity and/or pore morphology. Potential systematic errors and their interrelations are discussed further in the Appendix in the context of differences in X-ray CT results obtained with 9.25 μm and 3.00 μm voxel edge lengths. Additional error in the X-ray CT measurements associated with the reconstruction and image process have been partially quantified – the contribution of threshold value is small compared to the difference between X-ray CT and Archimedes measurements. There are, however, still unquantified uncertainties remaining in the X-ray CT process, which may contribute to the observed differences in measured porosity.

5.2. Acoustic Nonlinearity and Loss

As described in Secs. 4.3.2 and 4.3.3, the measured nonlinearity and loss are positively correlated with porosity (determined with the Archimedes method) with *p*-values less than 0.025 (Tables 4 and 5), except for the weaker correlation for the nonlinearity of specimens with the C orientation (*p*-value = 0.067). However, significant differences in linear-regression parameters of nonlinearity and loss *vs.* porosity for specimens containing material only from the upper half of the AM build (B orientation, Fig. 2) and specimens containing material from the lower half of the build (A and C orientations) indicate that defect parameters other than the volume fraction of pores contribute to the correlations and vary with height in the build.

There is actually little reason to expect that pores directly introduce substantial nonlinearity or loss in the specimens studied here. Note that, unlike attenuation of propagating waves, the loss of resonant acoustic modes is unaffected by scattering from pores (which can only affect vibrational patterns and resonant frequencies) and is, instead, determined by anelastic or viscoelastic effects [27]. Complex pore geometries can lead to hysteretic internal surface contact under acoustic stress and associated nonlinearity and anelasticity [32, 33]. Park *et al.* [34] assumed that this was the dominant physical mechanism for correlations of nonlinearity with laser power in a study of additively manufactured stainless steel with relatively high porosity (1.1 % to 7.0 %) and complex pore geometries (including entrapped powder). However, as described in the Appendix, X-ray CT data on the specimens studied here reveal few pores with such complex geometries and none with entrapped powder. SEM images (Fig. 12) also show no evidence for entrapped powder and support the conclusion that few pores have internal contacting surfaces. In the absence of hysteretic surface contact within pores, molecular dynamics calculations [35] of Fe have demonstrated a dependence of nonlinearity on

the volume fraction of approximately spherical pores with diameters of a few nanometers. However, this dependence was found to be opposite in sign and approximately an order of magnitude smaller than that shown in Fig. 8. We are not aware of similar calculations having been performed on aluminum or other FCC metals.

On the other hand, there are several reasons to expect that dislocations substantially contribute to nonlinearity and anelasticity of the specimens studied here. Bellotti [36] found a high correlation of nonlinearity with geometrically necessary dislocation (GND) density (determined from electron backscatter diffraction) in AM stainless steel. The literature on conventional metals includes many examples of dislocations being a major source of weakly frequency-dependent anelasticity and nonlinearity in metals at ambient temperatures, consistent with the Granato-Lücke "string" model of dislocation damping [37], the model of dislocation nonlinearity by Hikata *et al.* [38], and subsequent models of dislocation nonlinearity including orientation dependence [39–41]. As predicted by these theories, point defects and precipitates are found to reduce nonlinearity and anelasticity [27, 42–46], because they introduce pinning points that inhibit dislocation movement under acoustic stress. We suggest that differences in dislocation density and/or pinning are the principal defect parameters contributing to the variations in nonlinearity and loss shown in Figs. 8 and 10. Under this hypothesis, the observed correlations of acoustic characteristics with porosity could arise from either spatial variations in dislocation parameters in the vicinity of pores or more global differences in dislocation parameters and porosity that are each dependent on laser power during the build (Table 1). One additional factor to note with respect to this hypothesis is that the lack of second phases in the commercially pure AM aluminum eliminates the possibility of variations in phase fractions being a factor in the correlations of nonlinearity and loss with porosity.

Another feature to note in comparing the current results with previous NRS results on stainless steel [22] and conventional aluminum [21] is the sign of the shifts in resonant frequency with increasing vibrational amplitude. Figure 5 shows that the resonant frequency decreases with increasing RF amplitude on the sensing coil (*i.e.*, the frequency increases with time as vibrations decay during ringdown). The sign of this amplitude dependence is the same as that reported for cast Al (0.2% Zn) [21] and opposite to that reported for commercial 7075-T6 aluminum [21] (with much higher concentrations of alloying elements) and additively manufactured 17-4 stainless steel [22]. The negative slope of frequency *vs.* amplitude found for all of the AM aluminum specimens in this study is consistent with nonlinearity being dominated by the lowest-order (quadratic) nonlinear term in the classical stress/strain relation [47], and positive slopes observed in the NRS measurements of 7075-T6 Al and AM stainless can be attributed to higher-order terms in the stress/strain relation [21, 47].

Acoustic nonlinearity and loss are found to decrease with time during ultrasonic excitation, as illustrated in Figs. 6 and 9. This behavior suggests that defects contributing to nonlinearity and loss change in some way under acoustic excitation, which is surprising (and, perhaps, unprecedented) for acoustic measurements at inspection levels. The fact that, with a couple of exceptions, the nonlinearity and loss are not found to change significantly during pauses in excitation on the order of an hour indicates that material changes during acoustic excitation are not primarily thermally driven. Under the assumption that the principal nonlinear/anelastic elements are dislocations, one possible explanation for the observed time dependence is that the oscillation of dislocations under acoustic stress leads to movement of point defects over nanometer-scale distances towards lower-energy configurations, providing greater dislocation pinning.

With respect to application of the phase-sensitive NRS technique to qualification of AM parts in industrial environments, one may wonder whether the observed time dependence of nonlinearity/loss and associated material changes would be a problem. We do not see this as a likely practical limitation of the technique because of the speed with which measurements can be performed. Acquisition of a waveform for an individual measurement can be accomplished in just a few seconds. The most significant factor determining the time required for a measurement of an AM part is likely to be finding the approximate frequency of the target mode, which will be affected by variations in dimensions and porosity-dependent elastic constants. If, for example, nominally identical AM parts have as-built dimensional tolerances on the order of 1 %, we anticipate that the time required to nearly optimize excitation of a target mode would be approximately a minute. Note that, with tone-burst excitation, it is not necessary to acquire a time-consuming high-resolution frequency scan to identify the frequency of a resonant mode, because of the finite bandwidth of the tone burst. The Fourier transform of a driving tone burst of duration T_0 from a gated sine wave at frequency f_{ref} is approximately a sinc function with its first pair of minima at $f_{\mathrm{ref}} \pm 1/T_0$. Therefore, with a burst width on the order of a millisecond, Fourier transforms of received waveforms with just a few values of f_{ref} can be employed to rapidly determine the approximate frequency of a resonance within a range on the order of 10 kHz, and the procedure described in Sec. 3.1.6 can then be used to fine tune f_{ref}.

An additional observed effect, not described here, is a dependence of nonlinearity and loss on the symmetry of acoustic displacement patterns relative to the build plane. An exploration of this effect will be pursued in a subsequent report.

6. Conclusion

This study demonstrates sensitivity of acoustic nonlinearity and loss to small changes in porosity at industrially relevant levels (less than half a percent) in commercially pure AM aluminum built in an L-PBF system with several levels of laser power. The noncontacting phase-sensitive NRS technique employed for these measurements offers

advantages of adaptability to complex part geometries and short inspection times for industrial qualification of additively manufactured metal parts of arbitrary size.

Significant differences in linear-regression parameters of nonlinearity/loss *vs.* porosity for specimens containing material only from the upper half of the AM build and specimens containing material from the lower half of the build indicate that material parameters other than the volume fraction of pores contribute to the correlations. Since the commercially pure specimens are single-phase, variations in phase fractions are eliminated as a possibility for material parameters contributing to the correlations of nonlinearity and loss with porosity. Dislocations are hypothesized as being the principal nonlinear/anelastic elements, with the observed correlation of acoustic characteristics and porosity arising from either a dependence of dislocation parameters on proximity to pores or parallel dependence of porosity and dislocation parameters, thoughout the material, on L-PBF laser power. While this hypothesis is considered credible on the basis of published literature on dislocation effects in conventional and AM metals and a lack of SEM or X-ray CT evidence for potentially hysteretic surfaces in the specimens, no evidence directly supporting this hypothesis is presented in this report.

Nonlinearity and loss are found to decrease with time during acoustic excitation of a selected resonant mode, while being affected relatively little (with a couple of exceptions) by pauses in excitation of an hour or less. This behavior indicates that resonant acoustic excitation at the inspection levels employed in this study changes the material without predominant involvement of thermal excitation. This remarkable effect is not anticipated to be a problem for application of NRS in industrial AM part qualification because of the brief time required for measurements.

Measurements of porosity at the low levels in this study are found to be challenging. Archimedes measurements face a challenge of determining a reference value for the density of nonporous material with an uncertainty on the order of 0.01 %, and X-ray CT measurements face challenges in assessing systematic errors associated with resolution and sampling volume. Values of porosity of three representative specimens determined with these two techniques differ by 0.034 % to 0.15 % volume fraction, and the differences for the higher-porosity specimens are considered most likely to arise primarily from systematic error in X-ray CT. The values obtained with the two techniques show the same trends between specimens.

Further study of systematic errors associated with resolution and sampling volume in X-ray CT of AM aluminum is anticipated to be a focus of future work. Additional anticipated reports will focus on anisotropy of acoustic nonlinearity and loss and potential spatial correlations of pores, dislocation density, and impurity concentrations in AM aluminum.

7. Author Statement

Ward Johnson: conceptualization, methodology, software, acoustic data acquisition and analysis, writing. Jake Benzing: conceptualization, methodology, SEM data acquisition and analysis, writing. Orion Kafka: conceptualization, methodology, X-ray CT data acquisition and analysis, writing. Newell Moser: conceptualization, methodology, X-ray CT data acquisition and analysis, writing. Derek Harris: AM specimen fabrication and documentation. Jeremy Iten: conceptualization, AM methodology. Nik Hrabe: conceptuatization, methodology, review and editing.

References

[1] N. Hrabe, S. Daniewicz, and N. Shamsaei, NIST Advanced Manufacturing Series 100-4: Findings from the NIST/ASTM workshop on mechanical behavior of additive manufacturing components (National Institute of Standards and Technology, 2016), https://doi.org/10.6028/NIST.AMS.100-4.

[2] M. Gorelik, Additive manufacturing in the context of structural integrity, Int. J. Fatigue 94 (2017) 168–177.

[3] U. Zerbst, G. Bruno, J.-Y. Buffiere, T. Wegener, T. Niendorf, T. Wu, X. Zhang, N. Kashaev, F. Meneghetti, N. Hrabe, M. Madia, T. Werner, K. Hilgenberg, M. Koukolíková, R. Procházka, J. Dzugan, B. M oller, S. Beretta, A. Evans, R. Wagener, and K. Schnabel, Damage tolerant design of additively manufactured metallic components subjected to cyclic loading: State of the art and challenges, Prog. Mat. Sci. 121 (2021) 100786.

[4] J. M. Waller, B. H. Parker, K. L. Hodges, E. R. Burke, J. L. Walker, *Nondestructive Evaluation of Additive Manufacturing, State-of-the-Discipline Report NASA/TM—2014–218560* (NASA Langley Research Center, Hampton, VA, 2014)

[5] L. W. Koester, H. Taheri, T. A. Bigelow, P. C. Collins, and L. J. Bond, Nondestructive Testing for Metal Parts Fabricated Using Powder-Based Additive Manufacturing, *Materials Evaluation* 76 (4) (2018), pp.514–524.

[6] F. Honarvar and A. Varvani-Farahani, A review of ultrasonic testing applications in additive manufacturing: Defect evaluation, material characterization, and process control, Ultrasonics 108 (2020) 106227.

[7] E. Hanks, A.Palazotto, and D. Liu, Effect of surface roughness on ultrasonic inspection of electron beam melting ti-6AL-4V, J. Def. Anal. Logist. 3 (2) (2019) 131–141, doi: 10.1108/JDAL-12-2018-0019.

[8] A.-F. Obaton, B. Butsch, S. McDonough, E. Carcreff, N. Laroche, Y. Gaillard, J. B. Tarr, P. Bouvet, R. Cruz, and A. Donmez, Evaluation of Nondestructive Volumetric Testing Methods for Additively Manufactured Parts, in Structural Integrity of Additive Manufactured Parts, ed. N. Shamsaei, S. Daniewicz, N. Hrabe, S. Beretta, J. Waller, and M. Seifi (West Conshohocken, PA: ASTM International, 2020), 51–91. http://doi.org/10.1520/STP162020180099

[9] A.-F. Obaton, A. Van den Bossche, O. Burnet, B. Butsch, I. Zouggarh, F. Soulard, and W. Johnson, Novel or Improved NDE Inspection Capabilities for Additively Manufactured Parts, ASTM Progress in Additive Manufacturing 2020 (STP 1637) doi: 10.1520/STP163720200096.

[10] S. McGuigan, A. P. Arguelles, A.-F. Obaton, A. M. Donmez, J. Riviere, and P. Shokouhi, Resonant ultrasound spectroscopy for quality control of geometrically complex additively manufactured components, Addit. Manuf. 39 (2021) 101808.

[11] A.-F. Obaton, Y. Wang, B. Butsch, and Q. Huang, A non-destructive resonant acoustic testing and defect classification of additively manufactured lattice structures, Weld World 65 (2021) pp.361–371.

[12] E. Bozek, S. McGuigan, Z. Snow, E. W. Reutzel, J. Rivière, P. Shokouhi, Nonlinear resonance ultrasonic spectroscopy (NRUS) for the quality control of additively manufactured samples, NDT&E Int. 123 (2021) 102495.

[13] M. B. Prime, D. W. Shevitz, Linear and nonlinear methods for detecting cracks in beams, Proc. 14th Intnl. Modal Analysis Conference (1996) 1437–1443.
[14] K. E.-A. Van Den Abeele, A. Sutin, J. Carmeliet, P. A. Johnson, Micro-damage diagnostics using nonlinear elastic wave spectroscopy (NEWS), NDT&E Int. 34 (2001) 239–248.
[15] M. Muller, A. Sutin, R. Guyer, M. Talmant, P. Laugier, P. A. Johnson, Nonlinear resonant ultrasound spectroscopy (NRUS) applied to damage assessment in bone, J. Acoust. Soc. Am. 118 (2005) 3946–3952,
[16] P. Shokouhi, J. Riviere, C. R. Lake, P.-Y. Le Bas, T. J. Ulrich, Dynamic acousto-elastic testing of concrete with a coda-wave probe: comparison with standard linear and nonlinear ultrasonic techniques, Ultrasonics 81 (2017) 59-65.
[17] C. Espinoza, D. Feliú, C. Anguilar, R. Espinoza-González, F. Lund, V. Salinas, N. Mujica, Linear versus nonlinear acoustic probing of plasticity in metals: A quantitative assessment, Materials 11 (2018) 2217.
[18] K. M. S. Levy, J.-Y. Kim, L. J. Jacobs, Investigation of the relationship between classical and nonclassical ultrasound nonlinearity parameters and microstructural mechanisms in metals, J. Acoust. Soc. Am. 148 (2020) 2429.
[19] S. Haupert, G. Renaud, J. Rivière, M. Talmant, High-accuracy acoustic detection of nonclassical component of material nonlinearity, J. Acoust. Soc. Am. 130 (5) (2011) 2654.
[20] D. Pasqualini, K. Heitmann, J. A. TenCate, S. Habib, D. Higdon, and P. A. Johnson, Nonequilibrium and nonlinear dynamics in Berea and Fontainebleau sandstones: Low-strain regime, J. Geomphys. Res. 112 (2007) B01204.
[21] W. L. Johnson, Nonlinear reverberation spectroscopy with phase-sensitive superheterodyne reception, Mech. Syst. Signal Pr., 168 (2022) 108631.
[22] W. L. Johnson, J. F. Whiting, F. H. Kim, P. R. Heyliger, N. W. Hrabe, Resonant acoustic nonlinearity and loss in additively manufactured stainless steel, AIP Conf. Proc. 2102 (2019) 020008.
[23] J. Ciurana, L. Hernandez, J. Delgado, Energy density analysis on single tracks formed by selective laser melting with CoCrMo powder material, Int. J. Adv. Manuf. Technol. **68**, 1103 (2013).
[24] A. C. Eringen, E. S. Şuhubi, Elastodynamics, Vol. II, Academic, New York, 1975.
[25] W. L. Johnson, G. A. Alers, Noncontacting ultrasonic resonance measurement of transverse anisotropy in cylinders, in Review of Progress in Quantitative Nondestructive Evaluation, Vol. 14, ed. D. O. Thompson, D. E. Chimenti, Plenum, New York, 1995, pp. 1915–1921.
[26] E. Rubiola, Phase Noise and Frequency Stability in Oscillators, Cambridge University Press, Cambridge, 2009, p. 6.
[27] A. S. Nowick, B. S. Berry, Anelastic Relaxation in Crystalline Solids, Academic, New York, 1972.
[28] F. E. Jones and G. L. Harris, ITS-90 density of water formulation for volumetric standards calibration, J. Res. Natl. Inst. Stand. Technol. **97**, 335 (1992).
[29] Van der Walt, Stefan and Schönberger, Johannes L and Nunez-Iglesias, Juan and Boulogne, François and Warner, Joshua D and Yager, Neil and Gouillart, Emmanuelle and Yu, Tony, scikit-image: image processing in Python, Peer **2**, e453 (2014).
[30] Cakmak, Ercan and Bingham, Philip and Cunningham, Ross W. and Rollett, Anthony D. and Xiao, Xianghui and Dehoff, Ryan R., Non-destructive characterization of additively manufactured components with x-ray computed tomography for part qualification: A study with laboratory and synchrotron x-rays, Mater. Charact. **173**, 110894 (2021).
[31] W. Xu, L.P.Davila, Size dependence of elastic mechanical properties of nanocrystalline aluminum, Mat. Sci. Eng. A, vol. 692 (2017).
[32] M. A. Biot, Nonlinear and semilinear rheology of porous solids, J. Geophys. Res. 78 (1973) 4924–4937.
[33] D. M. Donskoy, K. Khashanah, and T. G. McKee, Nonlinear acoustic waves in porous media in the context of Biot's theory, J. Acoust. Soc. Am. 102 (1997) 2521.
[34] S.-H. Park, S. Choi, D.-G. Song, and K.-Y. Jhang, Microstructural CCharacterization of additively manufactured metal components using linear and nonlinear ultrasonic techniques, Materials 15 (2022) 3876.
[35] W. Setyawan, C. H. Henager, Jr., and S. Hu, Nonlinear ultrasonic response of voids and Cu precipitates in body-centered cubic Fe, J. Appl. Phys. 124 (2018) 035104.
[36] A. Bellotti, J.-Y. Kim, J. E. Bishop, B. H. Jared, K. Johnson, D. Susan, P. J. Noell, and L. J. Jacobs, Nonlinear ultrasonic technique for the characterization of microstructure in additive materials, J. Acoust. Soc. Am. 149 (2021) 158.
[37] A. Granato and K. Lücke, Theory of mechanical damping due to dislocations, J. Appl. Phys. 27 (1956) 583.
[38] A. Hikata, B. B. Chick, and C. Elbaum, Dislocation contribution to the second harmonic generation of ultrasonic waves, J. Appl. Phys. 36 (1965) 229–236.
[39] W. D. Cash and W. Cai, Dislocation contribution to acoustic nonlinearity: The effect of orientation dependent line energy, J. Appl. Phys. 109 (2011) 014915.
[40] Z. Chen and J. Qu, Dislocation-induced acoustic nonlinearity parameter in crystalline solids, J. Appl. Phys. 114 (2013) 164906.
[41] J. Zhang and F.-Z. Xuan, A general model for dislocation contribution to acoustic nonlinearity, EPL 105 (2014) 54005.
[42] G. A. Alers and D. O. Thompson, Dislocation contributions to the modulus and damping in copper at megacycle frequencies, J. Appl. Phys. 32 (1961) 283.
[43] G. Gremaud, Dislocation-point defects interactions, in Mechanical Spectroscopy, Materials Science Forum, ed. R. Schaller, G. Fantozzi, G. Gremaud, Vol. 366—368, Chapter 3.3, Trans Tech Publications, Switzerland (2001) 178–-247, https://doi.org/10.4028/www.scientific.net/MSF.366-368.178.
[44] M. Hirao and H. Ogi, Electromagnetic acoustic transducers: Noncontacting ultrasonic measurements using EMATs, 2nd Edition, Springer, Japan, 2016.
[45] W. Johnson, Ultrasonic dislocation dynamics in Al (0.2 at.% Zn) after elastic loading, Mat. Sci. Eng. A309–310 (2001) 69–73.
[46] D. C. Hurley, D. Balzar, and P. T. Purtscher, Nonlinear ultrasonic assessment of precipitation hardening in ASTM A710 steel, J. Mater. Res. 15 (2000) 2036–2042.
[47] A. H. Nayfeh, D. Mook, Nonlinear Oscillations, Wiley-VCH, Weinheim, 2004, p. 55.

A. Appendix: Uncertainties in X-ray CT measurements

Additional details about the X-ray CT results, including the lower magnification (9.25 μm voxel-edge length) measurements mentioned in Section 3.3, are summarized here. Examples of 3D renderings with lower magnification are shown in Fig. 13, and Table 6 presents the porosities of specimens 1-B, 8-B and 11-A determined with this magnification, along with previously presented higher-magnification results (Table 3).

There are multiple factors associated with X-ray CT measurements and post-processing that can affect the final estimate of porosity. For example, the threshold value used to segment the reconstructed images is a user-defined value and can impact the shape and size of the pores, at least within the resolution of the X-ray CT data (see Fig. 14). Filtering (e.g., smoothing and denoising) also involve user-selected parameters that can marginally impact the overall results. We expect systematic errors associated with these factors to be relatively consistent between low and high magnification measurements.

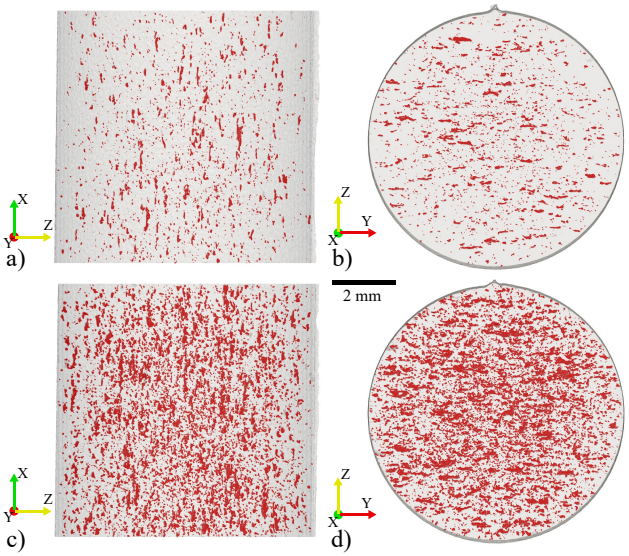

Figure 13: Three-dimensional isometric renderings from X-ray CT with 9.25 μm voxel edge length, showing two orthogonal views of two different specimens with partial transparency: (a-b) Specimen 1-B which has relatively low porosity, and (c-d) Specimen 8-B, which has relatively high porosity. The entire diameter of excised aluminum sample is represented here. The metal sample has been made translucent, and the fully enclosed pores are highlighted in red. In effect, all of the pores are projected onto the orthogonal views. The build direction during the AM process is along $\hat{z}$.

Table 6
Percent porosity as measured with X-ray CT at two resolutions: a low-magnification resolution utilizing a voxel-edge length of 9.25 μm, and a high-magnification resolution utilizing a voxel-edge length of 3.00 μm.

ID	Low-Mag. Porosity (%)	High-Mag. Porosity (%)
1-B	0.060	0.080
8-B	0.267	0.215
11-A	0.070	0.178

Another challenge is related to volumetric sampling uncertainty. In the measurement, there is a trade-off between total volume sampled and voxel-edge length. For example, with a detector size of 1000 pixels × 1000 pixels, one can either image the whole volume at a larger edge length (*i.e.*, 9.25 μm/voxel-edge) or measure a subset of the total specimen at shorter edge length (*e.g.*, 3.00 μm/voxel-edge). The shorter edge length more accurately captures the smaller pores, but requires a selection of a subvolume that is reasonably representative of the full sample. Both the size of the subvolume, dictated by the specified voxel-edge length, and the location of the subvolume must be considered when seeking a representative subvolume. For these aluminum samples, the size of pores is found to vary greatly. An abundance of both micro-pores (several micrometers in diameter) and meso-pores (100s of micrometers in diameter) are observed. A coarser resolution in X-ray CT

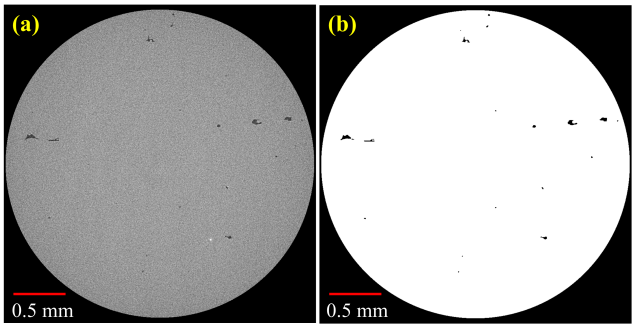

Figure 14: (a) An example of a reconstructed grey-scale image-slice of specimen 1-B obtained with X-ray CT with a voxel-edge length of 3.00 μm/pixel. (b) binary image determined from an application of Otsu global thresholding to the grey-scale image, where white pixels represent metal and black pixels represent voids.

Table 7
Higher resolution (3.00 μm) data quantifying the measured voids.

ID	Number of Voids	Mean Eqv. Sphere Diameter (μm)
1-B	3051	14.4
8-B	6613	15.1
11-A	15050	8.1

helps to ensure large pores are more fully contained within the field-of-view but has the drawback that small pores are no longer detectable, as illustrated in Fig. 15. Because of this effect, increasing the measurement resolution will generally tend to an increase in extracted porosity for a given subvolume, as more small pores are captured. However, due to the image processing required to extract values of porosity, it is also possible that, with very complex pore geometries, the "smearing" effect of a coarser resolution will drive complex shapes towards geometries closer to elliptical, which contain more empty space. In the X-ray CT data obtained in this study, the majority of pores are not found to have highly complex shapes, which is consistent with the SEM-based results (Fig. 12). There is, for example, no evidence for unmelted powder within pores similar to that which we previously observed in AM 17-4 stainless steel [22]. Therefore, we consider sampling error, rather than resolution error, to be the most likely driver for the decrease in extracted porosity of specimen 8-B that is observed when going from 9.25 μm to 3.00 μm voxel edge length (Table 6).

For specimen 11-A, analysis of the mean equivalent sphere diameter (Table 7) indicates that most pores are below the voxel edge length of the coarser measurement. This result and the fact that the higher resolution scan of this specimen yields a higher porosity (Table 6) are consistent with the large discrepancy between low and high resolutions measurements of this specimen being primarily driven by resolution limits.

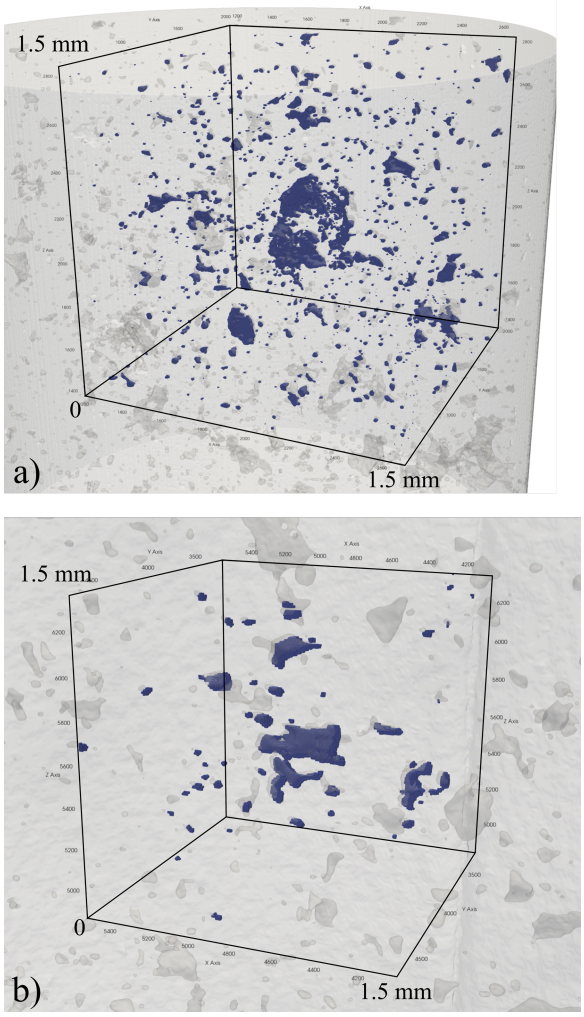

Figure 15: Specimen 11-A: a) Example close-up view of pores at 3.00 μm voxel-edge length (note that the boundaries of the scanned cylinder are visible on the top and side of the image); b) Example close-up view of a similar region of material at 9.25 μm voxel-edge length. Smaller pores and volumetric shape details are lost at lower resolution.